Fractal structure and nano-precipitates break comprehensive performance limits of CuCrZr alloys

Kaixuan Zhou [a,1], Yonghao Zhao [a,b,1,*], Hongzhen Dong [a], Qingzhong Mao [a], Shenbao Jin [c], Man Feng [c], Ruisheng Zhang [a], Shunqiang Li [a], Jizi Liu [a,c,*]

[a] *Nano and Heterogeneous Materials Center, Nanjing University of Science and Technology, Nanjing 210094, China*
[b] *School of Materials Science and Engineering, Hohai University, Changzhou 213200, China*
[c] *Center of Analytical Facilities, Nanjing University of Science and Technology, Nanjing 210094, China*

ARTICLE INFO

ABSTRACT

Modern industrial materials are often required to have excellent comprehensive properties. Contact wire used in high-speed train needs possess high strength and toughness, high conductivity and wear resistance, which are often trade-off with each other. In this work, we constructed a fractal structure with high-density nano-precipitates in CuCrZr alloy via rotary swage plus aging, and break the strength, conductivity and ductility limits of existing Cu alloys. The CuCrZr alloy exhibits unprecedented comprehensive properties of a high ultimate tensile strength of 626 MPa, a ductility of 19% and an electrical conductivity of 82% international annealed copper standard (IACS). Microstructural analysis indicates that the fractal structure and high-density nano-Cr precipitates block and accumulate dislocations, but allow electrons to flow unimpededly along the axis of CuCrZr wire, resulting in the high toughness and conductivity. Our finding verifies fractal structure has the potential to obtain materials with super excellent comprehensive properties.

Introduction

The rapid development of human science and technology puts forward more and more stringent requirements for the comprehensive performance of materials, and these requirements often exceed the performance limits of the materials themselves. In this context, people have to search and design super materials with super comprehensive properties. Specifically, Cu contact wire used in high-speed trains are required to simultaneously have excellent comprehensive properties such as high strength, ductility and conductivity as well as wear resistance etc. High strength can allow high stringing tension and running speed of high-speed railway [1]. High conductivity can help to improve their energy efficiency and carbon neutrality [2]. Moreover, high ductility is critical to safety and reliability of the high-speed train, because it can avoid catastrophic fracture failure [3]. However, strength and ductility, strength and conductivity are often trade-off with each other, which bring challenges to Cu contact wire used in high-speed train [4].

The strength-ductility paradox of metals and alloys arises from dislocation-slip dominated plastic deformation [5,6]. The yield strength ($\sigma_{0.2}$) corresponds to the resistance to massive nucleation of dislocations, and inversely, the numerous dislocation nucleation is beneficial to the ductility [7]. Therefore, the four traditional strengthening mechanisms including grain refinement, deformation, solid solution and 2nd-phase particle strengthening increase the $\sigma_{0.2}$ by increasing the critical shear stress for slip initiation and more or less reduce ductility without exception [8,9]. Fortunately, ductility is also closely related with slip kinetics including dislocation propagation and reaction after yielding [10]. Such a subtle difference between $\sigma_{0.2}$ and ductility makes it possible to optimize strength and ductility [11]. Some strategies are thus proposed and obtained more or less success in improving strength and ductility of metals [12]. It must be recognized that different strategies are compared across borders, and strength and ductility are still in the shape of "banana" if these strategies are compared with themselves [13].

The fundamental mechanism that determines the strength and conductivity paradox is that all four strengthening mechanisms inevitably introduce lattice defects, which further lead to electron scattering,

---

Table 1

Chemical compositions of the CuCrZr alloy analyzed in direct-read spectroscopic analyzer. The elements detected in excess of 0.005% were listed.

Elements	Cr	Zr	Si	Sb	Fe	Zn	Total others	Cu
wt%	0.41	0.15	0.072	0.006	0.006	0.005	< 0.02	balance

reducing the conductivity [14]. In fact, strength and conductivity are not exactly the same thing because strength is related to dislocation behavior, and conductivity is related to electron motion, while the lattice defects used for strengthening happen to affect the movement of electrons at the same time. In fact, we need to find a structure that only blocks dislocations without scattering electrons.

In order to achieve the best comprehensive performance, after hundreds of millions of years, organisms have evolved fractal structure, which was first proposed by mathematician Lewis Fry Richardson. It is a geometric concept referring to the infinite repetition of similar morphology from macro to micro [15]. The fractal structure is widely existing in nature, such as trunk branches, leaf veins, romaine cauliflower, biological bones and muscles, and so on. Compared with biological fractal structure, man-made materials are simple and rarely have complex multi-level fractal structure. Here we constructed a fractal structure in CuCrZr alloys and obtained an unprecedented combination of a high ultimate tensile strength (UTS) of 626 MPa, a ductility of 19% and an electrical conductivity of 82% international annealed copper standard (IACS) at room temperature. Our results can provide a new strategy for developing high comprehensive performance materials with both super mechanical and conductive properties.

Experimental section

Materials preparation

The as-received 50 × 50 × 300 mm rectangular blocks CuCrZr alloys were prepared by smelting and heat forged. The chemical composition of the CuCrZr alloy was tested by a direct-read spectroscopic analyzer-Q4 TASMAN 130 (Bruker, Germany), results of the analysis are shown in Table 1. The CuCrZr alloy were homogenized in an air circulated furnace at 1000 °C for 2 h followed by water quenching, it was then prepared into Ø18 × 300 mm rods by machining, the microstructure of the alloy after the ST was shown in Fig. S1, Supporting Information, with an average grain size of 176 μm, and with a relatively random orientation. The CuCrZr rods were then rotary swaged at room temperature through multiple pass down to Ø5.2 mm, corresponding to the equivalent strain of 2.5 (RS$_{2.5}$), as calculated by the formula ($\varphi = \ln(A_0/A)$, where A_0 and A are the initial and final cross-sectional areas. Each pass reduces the diameter of the rod by approximately 0.3 mm, the rotation speed is 110 r/min. Subsequently, a 1-hour aging was performed at 573, 723, and 873 K, named as 573 K/1 h, 723 K/1 h, and 873 K/1 h, respectively.

Mechanical and electrical properties tests

Uniaxial tensile tests were performed using a Instron 5982 tester with a strain rate of 1×10^{-3} s^{-1} at room temperatures. The dog-bone-shaped tensile specimens with dimensions of 0.8 × 2 × 5 mm^3 were cut from the central position of swaged rods with gauge length along the swaging direction. The strain was measured by using a standard non-contacting video extensometer. Three tensile specimens were tested to obtain reliable results.

The conductivity test was performed using a four-point probe resistivity tester at 20 °C. The specimen has a dimension of 0.8 × 0.8 × 25 mm^3 with longitudinal direction parallel to the swaging direction.
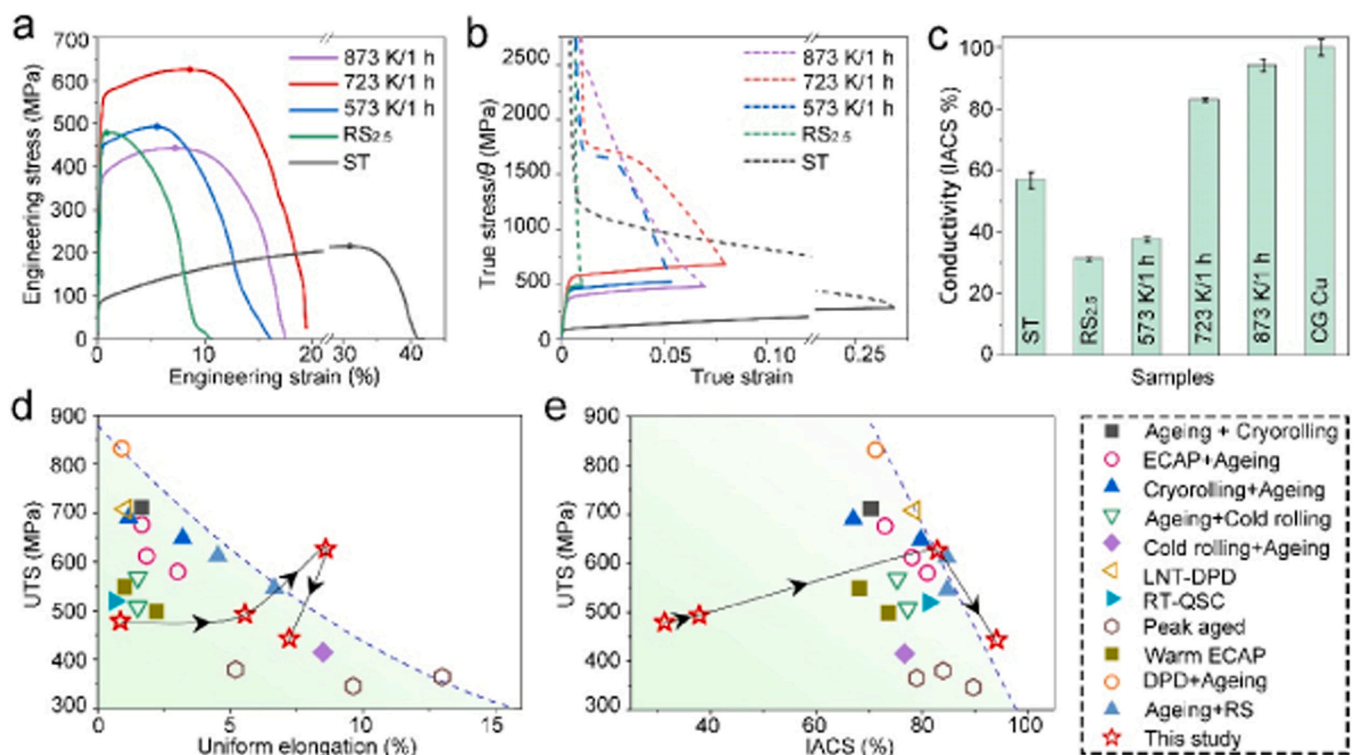
Fig. 1. Tensile and conductive properties of CuCrZr alloy as well as summaries of literature data. (a) The quasi-static uniaxial tensile curves. (b) The curves of true stress (solid line)/work hardening rate (dashed line) versus true strain. (c) The conductivity of CuCrZr alloy measured at 20 °C. (d) The UTS versus ε_u and (e) UTS versus conductivity of the present data as compared with the literature values, respectively.
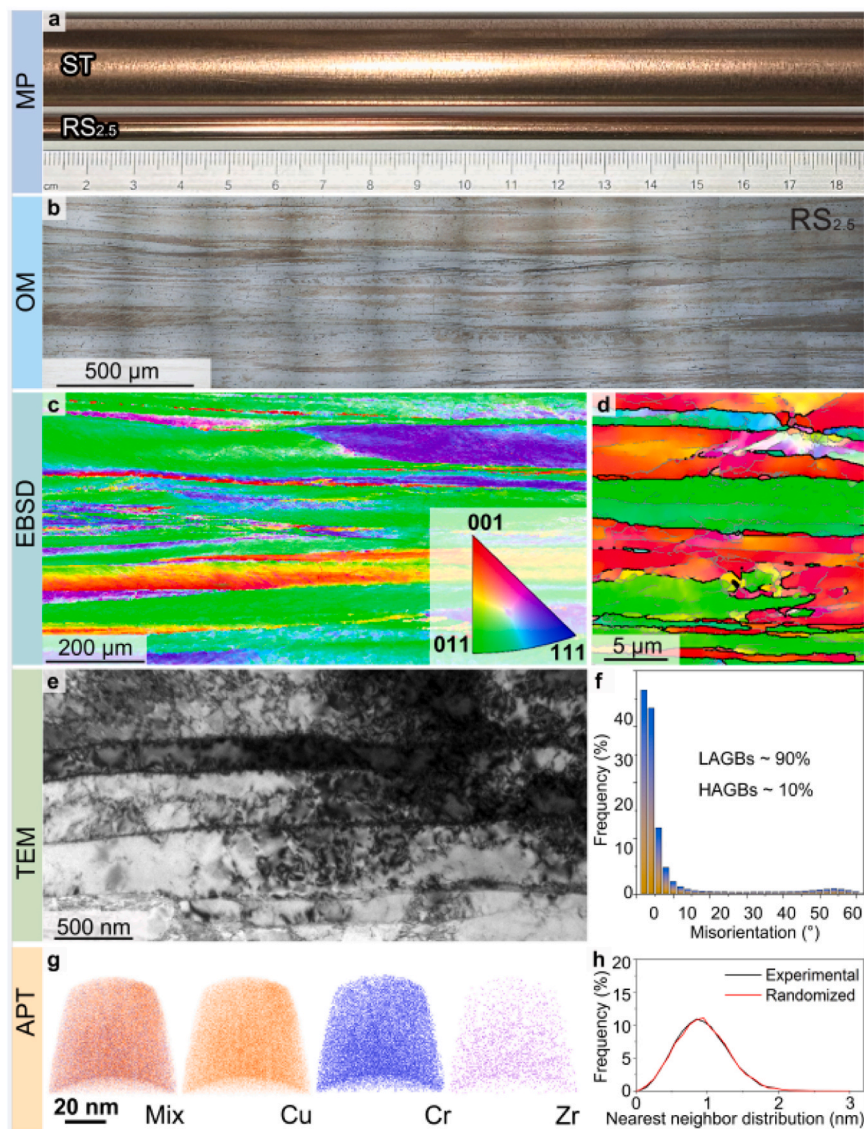
Fig. 2. Macro picture and microstructures of the sample RS$_{2.5}$. (a) Picture of initial and swaged CuCrZr alloy. (b) Side-view metallographic photos. (c) The inverse pole figure (IPF) map of side-view, inset is the legend of the IPF map. (d) Enlarged view of the local area in c, it also includes LAGBs (grey line) and HAGBs (black line). (e) Bright-field TEM image of side-view. (f) Grain boundaries misorientation angle distributions. (g) Reconstruction results of the APT tip of Cu (orange), Cr (blue), Zr (pink). (h) Nearest neighbor distribution of Cr in randomized and experimental.

The value of conductivity δ is determined by $\delta = 1/\rho = RS/l$, where ρ is the electrical resistivity, R is the resistance, S is the cross-sectional area, and l is the length between two voltage probes.

Microstructure characterizations

X-ray diffraction (XRD) measurements were performed on a Bruker-AXS D8 diffractometer with Cu Kα radiation. The 2θ angle ranged from 40 to 100°, the scanning step size is 0.02°, and each step stays for 2 s.

Electron back-scattering diffraction (EBSD) analysis was performed on a Zeiss Auriga focused ion beam/scanning electron microscope equipped with a fully automatic Oxford Instruments Aztec 2.0 EBSD system (AZtecCrystal Software). Samples used for EBSD were first sandpaper polished and mechanically polished before electropolished on Buehler ElectroMet@4 with 25% H$_3$PO$_4$ +25% absolute alcohol + 50% deionized water electrolyte, voltage of 8 V and polishing time of 30–60 s. The scanning step size is 10 μm for sample ST, 1.5 μm for sample RS$_{2.5}$ and subsequent annealed samples.

Transmission electron microscope (TEM) (Titan G2 60–300 TEM)

was used for characterization the microstructure of the samples with a voltage of 300 kV. The samples used for TEM underwent machining and sanding to obtain 60 μm thick discs. Twin-jet polishing in an electrolyte of 25% H$_3$PO$_4$ +25% absolute alcohol + 50% deionized water at about −8 °C, the residual surface phosphate was then removed with ion milling (Gatan 695).

Atom probe tomography (APT) characterization was performed on a local electrode atom probe (LEAP4000X Si), use laser as excitation source. The APT specimens were prepared by the standard two-step electro-polishing method. The reconstruction and quantitative analysis of APT data were conducted on CAMECA Visualization and Analysis Software (IVAS 3.6.12).

Results

Mechanical and electrical properties

The CuCrZr wire with fractal structure was fabricated by rotary swaging (RS) of as-received solution treated (ST) alloy and the high-
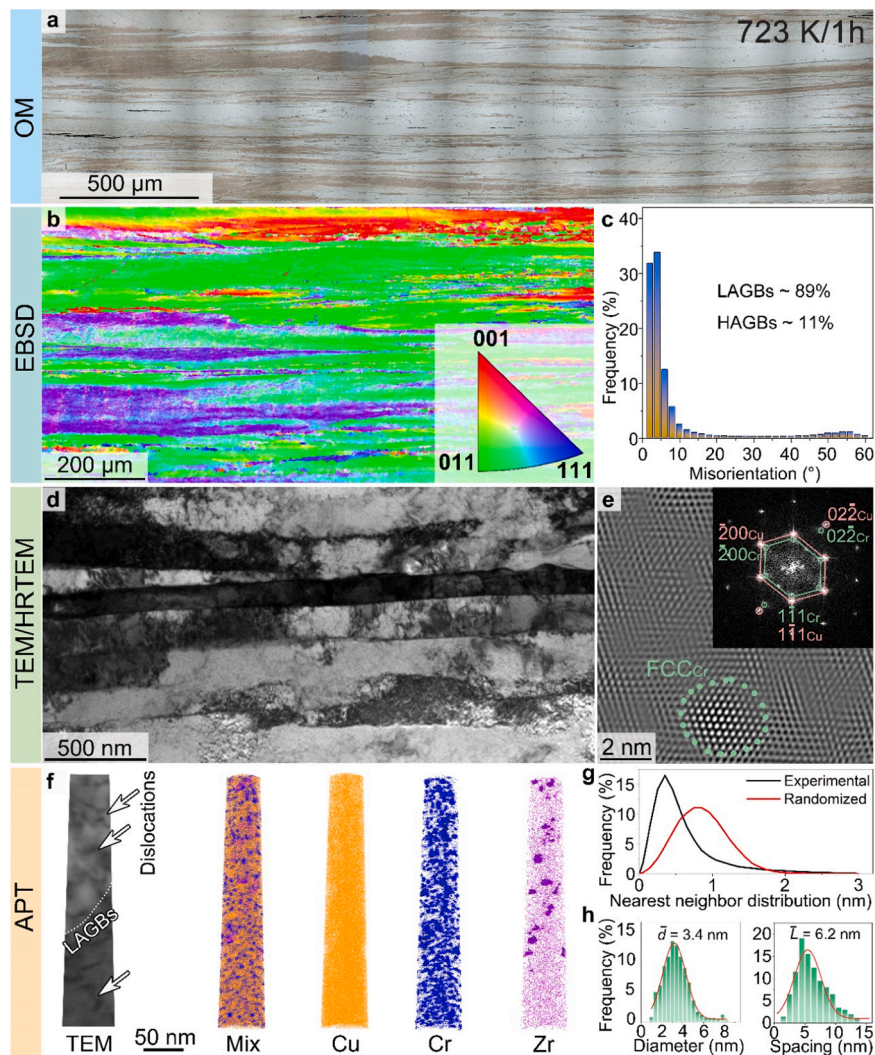
Fig. 3. Microstructures of the sample 723 K / 1 h. (a) Side-view metallographic photos. (b) The IPF map of side view, inset is the legend of the IPF map. (c) Grain boundaries misorientation angle distributions. (d) Bright-field TEM image of side view. (e) Inverse Fourier transform of high-resolution TEM image for Cr precipitate, the inset is the Fourier transform image. (f) Bright-field TEM image and reconstruction results of the APT tip of Cu (orange), Cr (blue), Zr (pink), white arrows point to dislocations. (g) Nearest neighbor distribution of Cr in randomized and experimental. (h) Distribution of diameters of Cr precipitates.

density nano-Cr precipitates was introduced via subsequent aging at different temperatures (Material preparation for details). Quasi-static uniaxial tensile testing revealed that the sample ST have the lowest $\sigma_{0.2}$ of 85 MPa, UTS of 215 MPa, the maximum uniform elongation (ε_u) of 30% and elongation to failure (ε_f) of 40% (Fig. 1a and Table S1, Supporting Information) as well as a high work hardening ability (Fig. 1b). RS deformation with an equivalent strain of 2.5 increases $\sigma_{0.2}$ and UTS up to 476 MPa and 479 MPa, respectively, while reduces ε_u and ε_f down to 0.8% and 10.4%, respectively. Moreover, RS results in a rapid drop in work hardening rate (θ) to necking (Fig. 1b). The UTS and/or ε_u of the alloy were significantly improved after aging at 573 K / 1 h, 723 K / 1 h, and 873 K / 1 h, among these, the sample 723 K / 1 h possesses the best combination of UTS (626 MPa) and ε_u (8.6%). During the stage of uniform plastic deformation, sample 723 K / 1 h exhibits a high θ value and a slow decrease in θ (Fig. 1b), this is due to the high ability to accumulate dislocations, which is related to the cooperation between the recovery of dislocations during aging and the pinning effect of precipitates on dislocations.

The conductivity of the CuCrZr alloy was shown in Fig. 1c, where the annealed coarse-grain (CG) copper with a purity of 99.99% was also tested simultaneously to ensure the experimental accuracy (100% IACS). The conductivity of the ST alloy is 58% IACS,

and RS reduces it to 31% IACS, mainly due to dislocation accumulation. Subsequent aging gradually increases the conductivity to 39% IACS (573 K/1 h), 82% IACS (723 K/1 h) and 95% IACS (873 K/1 h), respectively, due to the reduction of dislocation density and the precipitation of the nano-precipitates in the supersaturated solid solution.

The relationship between UTS versus ε_u, and UTS versus IACS of the CuCrZr alloys in previous studies are summarized in Fig. 1d,e, respectively [16–25]. The dashed box on the right shows the legend of Fig. 1d, e. A combination of plastic deformation and aging treatment was used in almost all studies, while the methods of plastic deformation are varied, including rolling, equal channel angular pressing (ECAP), dynamic plastic deformation (DPD) and quasi-static compression (QSC), deformation temperature also varies, such as liquid nitrogen temperature (LNT), room temperature, and elevated temperature. The pentagonal star symbol in the Fig. 1d,e represents the data of the RS$_{2.5}$, 573 K/1 h, 723 K/1 h, and 873 K/1 h samples in this study, and the arrow points in the direction of increasing the aging temperature. It is interesting that the combination of UTS and ε_u of our 723 K/1 h sample stands out of all other literature data with a typical "banana" curve (Fig. 1d). Moreover, the UTS-conductivity combination data points also reach the border of the best data in literature (Fig. 1e).
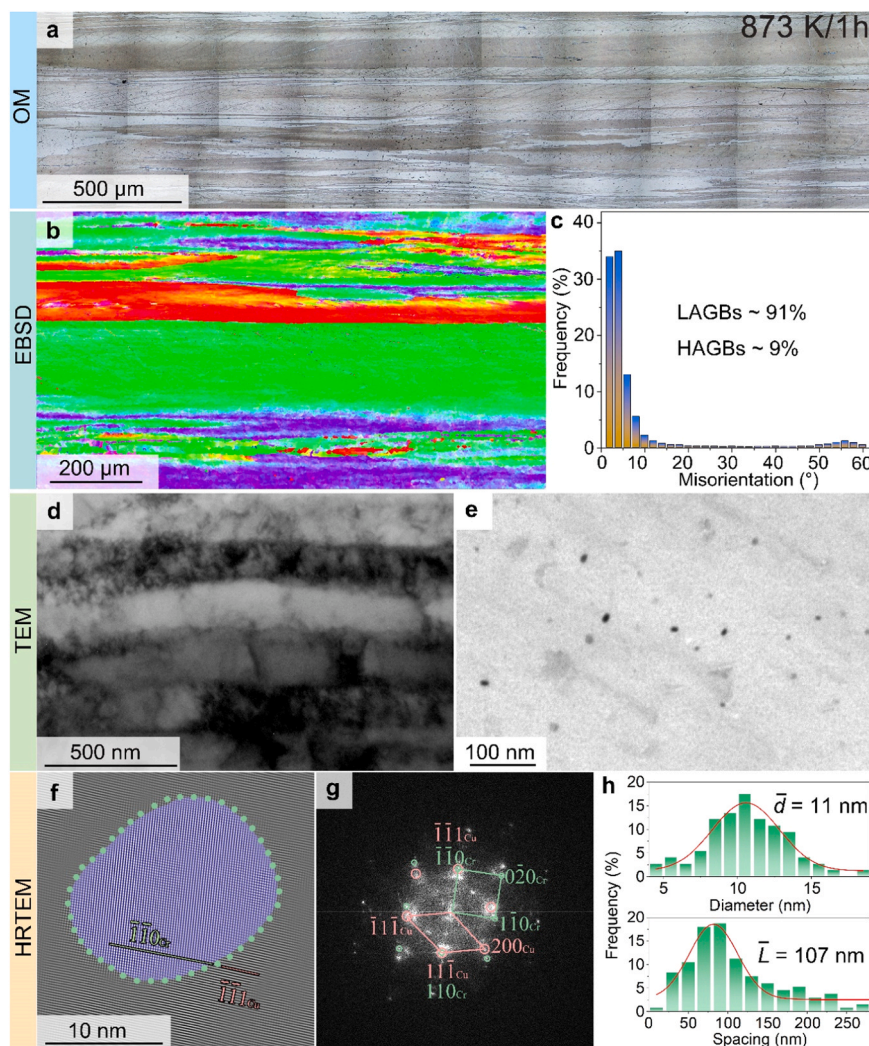
Fig. 4. The microstructure of sample 873 K/1 h. (a) Side-view metallographic photos. (b) The IPF map of side view, inset is the legend of the IPF map. (c) Grain boundaries misorientation angle distributions. (d) Bright-field TEM image of side view. (e) Locally enlarged bright-field TEM image. (f) The inverse Fourier transform image of the Cr precipitate. (g) The Fourier transform pattern. (h) The diameter and spacing distribution of the Cr precipitates.

Microstructure characterizations

EBSD characterization revealed that the ST CuCrZr alloy has a random grain orientation and an average grain size of 176 μm (Fig. S1, Supporting Information). The RS deformation elongated the initial equiaxed coarse grains to fibrous grains with an average length of 540 μm along the rod axis, and an average width of 11 μm perpendicular to the rod axis, respectively (Fig. 2b,c and Fig. S2a,b, Supporting Information). Further magnified EBSD and TEM analysis found the elongated grains bordered with high-angle grain boundaries (HAGBs) were further composed of a large amount of fibrous sub-grains with low-angle grain boundaries (LAGBs), a proportion of up to 90% (Fig. 2f), and an average length of 8 μm as well as an average width of 166 nm (Fig. 2d,e and Fig. S2c,d, Supporting Information). The above multi-level fiber structure is actually a typical fractal structure. Moreover, there are high-density dislocations within the sub-grains (Fig. 2e).

The more detailed texture information of the fractal structure CuCrZr was shown in Fig. S2e-l, Supporting Information, i.e., about 70% of <111> and 30% of <001> fiber textures along the RS direction. XRD further verified the above results (Fig. S2m,n, Supporting Information). From the top view of the wires, <111> oriented grains dominate accompanied with a small number of <200> oriented grains. While from the side view, <220> oriented grains dominated. APT results

(Fig. 2g) indicate that Cr and Zr elements in the RS CuCrZr alloys are uniformly distributed in the Cu matrix as solutes without precipitates or clusters, and Fig. 2h further indicates that the average nearest neighbor Cr ion distribution substantially coincides with the random distribution. In addition, the dislocation densities and lattice constant of the samples ST, RS$_{2.5}$, 573 K/1 h, 723 K/1 h, and 873 K/1 h were calculated based on the XRD results, as shown in Table S2 and Calculation S1, Supporting Information. RS enhanced dislocation density significantly from $1.4*10^{12}$ to $1.5*10^{15}$ m^{-2} without varying lattice parameter.

After ageing for 1 hour at 573 K, except for dislocation recovery, there were no significant changes in other microstructures including the grain/sub-grain morphology/size, fractions of HAGBs and LAGBs, and texture components, as shown in Fig. S3, Supporting Information. And so is the sample 723 K/1 h (Fig. 3a-d and Fig. S4, Supporting Information), however, Cr precipitation is the main characteristic. According to the Fourier transform of the high-resolution TEM image (Fig. 3e), the precipitated Cr and the Cu matrix have the same face centered cubic (FCC) structure, and have a completely coherent relationship, the lattice constant of Cr is slightly larger than that of the Cu matrix. APT results (Fig. 3f) show that high-density nano Cr precipitates are uniformly distributed in the grains, and the size is slightly larger at the dislocation and LAGBs. Fig. 3g further indicates that the average nearest neighbor Cr ion distribution deviates from the random distribution. The average
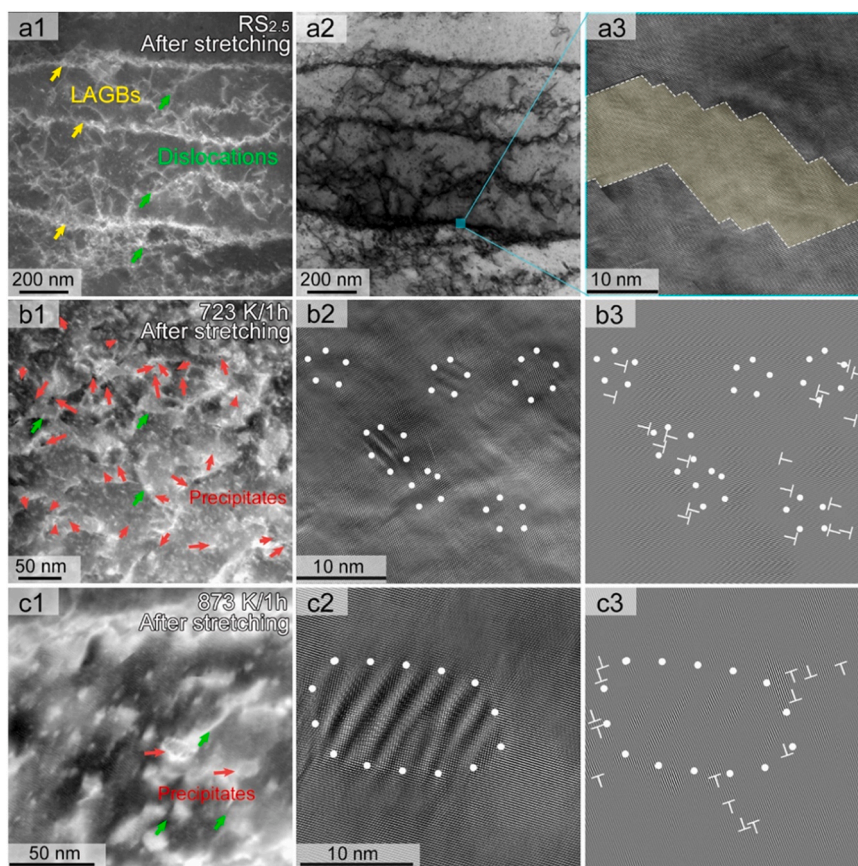
Fig. 5. The microstructure of samples RS$_{2.5}$, 723 K/1 h, and 873 K/1 h in the uniformly deformed area after stretching. (a1-a3) High-angle annular dark-field (HAADF), corresponding bright-field, and high-resolution TEM (HRTEM) images of sample RS$_{2.5}$. (b1-b3) HAADF, HRTEM, and corresponding inverse Fourier transform images of sample 723 K/1 h, (c1-c3) HAADF, HRTEM, and corresponding inverse Fourier transform images of sample 873 K/1 h. The green, yellow, and red arrows point to dislocations, LAGBs, and precipitates, respectively. The white dotted lines surround the precipitates and the symbol ⊥ indicates dislocations in HRTEM and inverse Fourier transform images.

diameter and spacing of the Cr precipitates were 3.4 nm and 6.2 nm, respectively (Fig. 3h). Zr element also precipitates in small amounts, adjacent to a few Cr precipitates located in dislocations or LAGBs. Moreover, the supersaturated Cr atoms in the matrix is fully precipitated during the aging, resulting in the lattice constant of 723 K/1 h being the same as that of annealed pure copper, and the dislocation density decreased to $9.6*10^{14}$ m^{-2} (Table S2, Supporting Information).

Aging at 873 K/1 h did not change the fractal structure either, such as texture components, grain morphology/size, fractions of HAGBs and LAGBs, and grain boundaries misorientation distribution (Fig. 4a-d). However, compared with sample 723 K/1 h, higher aging temperature changed the nucleation density and size of Cr precipitates (Fig. 4e,f), the average diameter and spacing of Cr precipitates were 11 nm and 107 nm, respectively (Fig. 4h). Moreover, the precipitates have a body centered cubic (BCC) structure and are semi-coherent with the copper matrix (Fig. 4f,g). The orientation relationship between BCC Cr precipitate and matrix was as follows:

$$[011]Cu//[001]Cr, (11\bar{1})Cu//(110)Cr \qquad (1)$$
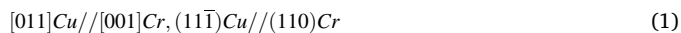
The close-packed plane of the Cr precipitation and Cu matrix is parallel, but the close-packed direction is not parallel. The precipitates have a typical Nishiyama-Wassermann (N-W) orientation relationship with the matrix [26–28]. The dislocation density decreased to $6.3*10^{14}$ m^{-2}, and the lattice parameter of Cu matrix is the same as pure Cu (Table S2, Supporting Information).

Deformation mechanisms

A high work hardening ability is crucial for good uniform elongation, as it can help delay local deformation (necking) under tensile stress. In order to investigate the deformation mechanism of samples RS$_{2.5}$, 723 K/1 h, and 873 K/1 h, the microstructure of the uniform deformation area after tensile deformation was characterized by TEM (Fig. 5). Firstly, due to the ε_u of sample RS$_{2.5}$ was only 0.8%, the microstructure before and after stretching did not differ much, i.e., a part of the dislocations self-organized into polygonal dislocation walls, and formed substructures or sub-grains with LAGBs within the slender grains, as shown in **Fig. 5**a1-a3. Then for the 723 K/1 h sample, high dislocation density and high-density precipitates were found inside the sub-grains (**Fig. 5**b1), HRTEM and inverse Fourier transform images show dislocations distributed within and around precipitates (**Fig. 5**b2,b3), indicating that coherent Cr precipitates can interact with the dislocations to enhance the accumulation of dislocations and thus the work hardening ability. Finally, for sample 873 K/1 h, the precipitates can also hinder dislocations, but the lower density of precipitates compared to sample 723 K/1 h results in lower work hardening ability, as shown in **Fig. 5**c1-c3.

Discussion

Fig. 6 schematically illustrates the microstructure evolution of CuCrZr during swaging and ageing. Among them, Fig. 6a, b, and c correspond to the ST, RS$_{2.5}$, and 723 K/1 h samples in this paper, respectively. The ST sample has a relatively uniform CG structure. After
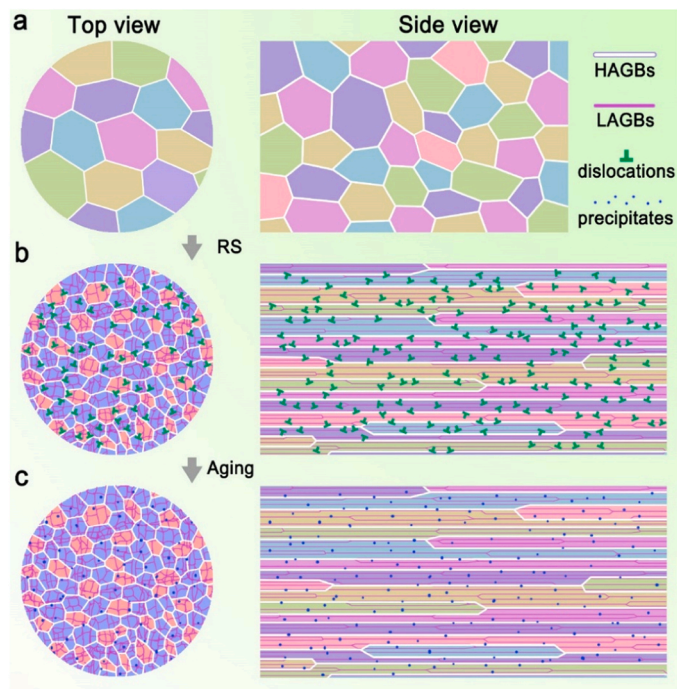
Fig. 6. Schematic illustration of structure evolution of CuCrZr alloy optimized by fractal structure and nano-precipitates. (a-c) Samples ST, RS$_{2.5}$, and 723 K/1 h, respectively.

the RS deformation, the grain size is greatly reduced in the radial direction, while in the axial direction, it was elongated to hundreds of micrometer or even millimeter range with high-density dislocations and LAGBs, forming a fractal structure. After 723 K/1 h aging, the dislocation density decreased significantly, and high-density Cr precipitates were produced.

In fractal structure, the LAGBs along the axis of the wires can effectively prevent the dislocation slip, thus improving the strength. It can also reduce the scattering effect of the interface to electrons in axis direction and improve the electrical conductivity. Nano-precipitates can increase the nucleation sites of dislocations, and can interact with moving dislocations, that is, they are cut or bypassed by dislocations to strengthen and toughen materials [7]. Based on this structure, the combination of excellent strength, elongation, and conductivity proves that our design has broad application prospects in materials used for one-dimensional conductivity.

Through detailed and reasonable estimation, we separated the strengthening mechanism components of each sample in this study. For the sample 723 K/1 h with the best comprehensive performance, dislocation strengthening and precipitation strengthening accounted for the majority, with their components reaching 56% and 36% of the total yield strength, respectively. For the 873 K/1 h sample, the larger diameter and spacing of precipitates greatly reduced the precipitation strengthening component, resulting in lower strength (Calculation S2, Supporting Information).

Factors such as texture, second phase size and distribution, grain size and shape, dislocation density, and lattice distortion have varying degrees of influence on conductivity. For CG pure Cu, HAGBs is the main lattice defect that affects the conductivity, and low grain boundaries density makes CG pure Cu have high conductivity (100% IACS). Although the fractal structure CuCrZr alloy we designed introduces a large number of dislocations that are harmful to conductivity, it makes its grain length along the wire direction even higher than the grain diameter of the sample ST, this greatly reduces the impact of HAGBs on conductivity while strengthening the alloy. This concept breaks the trade-off between strength and conductivity from an application

perspective. In fact, strength, ductility, and conductivity in this fractal structured material can be regulated by different aging treatments according to demand.

In industrial applications, not only material performance but also feasibility should be considered. Compared with many severe plastic deformation methods, RS has the characteristics of low cost and large sample size, this makes the CuCrZr alloy with fractal structure and nano-precipitates has a huge advantage in the application of contact wires in high-speed trains.

Conclusion

In short, we propose a design concept that uses fractal structure and nano-precipitates to optimize the overall performance under directional conditions. The CuCrZr wires with fractal structure along the axis of the wire rod were further prepared by RS, and the minimal dispersion nano-precipitates were obtained by annealing, and the excellent comprehensive properties of strength, ductility and conductivity were obtained, and it helps to be applied in the field of contact wires for high-speed trains.

CRediT authorship contribution statement

Man Feng: Methodology. **Ruisheng Zhang:** Methodology. **Shunqiang Li:** Methodology. **Kaixuan Zhou:** Writing – review & editing, Writing – original draft, Visualization, Methodology, Investigation, Formal analysis. **Hongzhen Dong:** Methodology, Investigation. **Qingzhong Mao:** Methodology, Investigation. **Jizi Liu:** Writing – review & editing, Project administration, Methodology, Funding acquisition, Formal analysis, Conceptualization. **yonghao zhao:** Writing – review & editing, Supervision, Investigation, Funding acquisition, Formal analysis, Conceptualization. **Shenbao Jin:** Investigation, Methodology.

Declaration of Competing Interest

The authors declare that they have no known competing financial interests or personal relationships that could have appeared to influence the work reported in this paper.

Data Availability

Data will be made available on request.

Acknowledgments

Appendix A. Supporting information

Supplementary data associated with this article can be found in the online version at doi:10.1016/j.nantod.2024.102234.

References

[1] C.Q. Huang, On contact wire line used in catenary of high speed wheel-rail electrified railway, China Railw. Sci. 22 (2001) 1–5.

[2] H. Yang, Z. Ma, C. Lei, L. Meng, Y. Fang, J. Liu, H. Wang, High strength and high conductivity Cu alloys: a review, Sci. China Technol. Sci. 63 (2020) 2505–2517.

[3] Q.Z. Mao, Y.S. Zhang, Y.Z. Guo, Y.H. Zhao, Enhanced electrical conductivity and mechanical properties in thermally stable fine-grained copper wire, Commun. Mater. 2 (2021) 1–9.

[4] Q.Z. Mao, Y.S. Zhang, J.Z. Liu, Y.H. Zhao, Breaking material property trade-offs via macrodesign of microstructure, Nano Lett. 21 (2021) 3191–3197.

[5] Y.H. Zhao, X.Z. Liao, S. Cheng, E. Ma, Y.T. Zhu, Simultaneously increasing the ductility and strength of nanostructured alloys, Adv. Mater. 18 (2006) 2280–2283.

[6] S. Cheng, Y.H. Zhao, Y.T. Zhu, E. Ma, Optimizing the strength and ductility of fine structured 2024 Al alloy by nano-precipitation, Acta Mater. 55 (2007) 5822–5832.

[7] P.V. Liddicoat, X.Z. Liao, Y.H. Zhao, Y.T. Zhu, M.Y. Murashkin, E.J. Lavernia, S. P. Ringer, Nanostructural hierarchy increases the strength of aluminium alloys, Nat. Commun. 1 (2010) 63.

[8] M.J. Starink, S.C. Wang, A model for the yield strength of overaged Al–Zn–Mg–Cu alloys, Acta Mater. 51 (2003) 5131–5150.

[9] E. Nes, T. Pettersen, K. Marthinsen, On the mechanisms of work hardening and flow-stress saturation, Scr. Mater. 43 (2000) 55–62.

[10] P.M. Anderson, J.P. Hirth, J. Lothe, Theory of Dislocations, Cambridge University Press, 2017.

[11] Y.H. Zhao, J.F. Bingert, X.Z. Liao, B.Z. Cui, K. Han, A.V. Sergueeva, Y.T. Zhu, Simultaneously increasing the ductility and strength of ultra-fine-grained pure copper, Adv. Mater. 18 (2006) 2949–2953.

[12] E. Ma, T. Zhu, Towards strength–ductility synergy through the design of heterogeneous nanostructures in metals, Mater. Today 20 (2017) 323–331.

[13] Y. Zhu, X. Wu, Heterostructured materials, Prog. Mater. Sci. 131 (2023) 101019.

[14] L. Lu, Y.F. Shen, X.H. Chen, L.H. Qian, K. Lu, Ultrahigh strength and high electrical conductivity in copper, Science 304 (2004) 422–426.

[15] J.C. Hunt, Lewis Fry Richardson and his contributions to mathematics, meteorology, and models of conflict, Annu. Rev. Fluid. Mech. 30 (1998) xiii–xxxvi.

[16] G.Y. Li, S.Y. Li, L. Li, D.T. Zhang, J.D. Wang, Y.X. Tong, A high strength and high electrical conductivity CuCrZr alloy prepared by aging and subsequent cryorolling, Vacuum 190 (2021) 110315.

[17] Y.X. Tong, Y. Wang, Z.M. Qian, D.T. Zhang, L. Li, Y.F. Zheng, Achieving high strength and high electrical conductivity in a CuCrZr alloy using equal-channel angular pressing, Acta Metall. Sin. Engl. 31 (2018) 1084–1088.

[18] R. Li, E. Guo, Z. Chen, H. Kang, W. Wang, C. Zou, T. Li, T. Wang, Optimization of the balance between high strength and high electrical conductivity in CuCrZr alloys through two-step cryorolling and aging, J. Alloy. Compd. 771 (2019) 1044–1051.

[19] S. Zhang, R. Li, H. Kang, Z. Chen, W. Wang, C. Zou, T. Li, T. Wang, A high strength and high electrical conductivity Cu-Cr-Zr alloy fabricated by cryorolling and intermediate aging treatment, Mater. Sci. Eng. A 680 (2017) 108–114.

[20] A. Meng, J. Nie, K. Wei, H. Kang, Z. Liu, Y. Zhao, Optimization of strength, ductility and electrical conductivity of a Cu–Cr–Zr alloy by cold rolling and aging treatment, Vacuum 167 (2019) 329–335.

[21] L.X. Sun, N.R. Tao, K. Lu, A high strength and high electrical conductivity bulk CuCrZr alloy with nanotwins, Scr. Mater. 99 (2015) 73–76.

[22] R. Mishnev, I. Shakhova, A. Belyakov, R. Kaibyshev, Deformation microstructures, strengthening mechanisms, and electrical conductivity in a Cu–Cr–Zr alloy, Mater. Sci. Eng. A 629 (2015) 29–40.

[23] Z.Y. Zhang, L.X. Sun, N.R. Tao, Nanostructures and nanoprecipitates induce high strength and high electrical conductivity in a CuCrZr alloy, J. Mater. Sci. Technol. 48 (2020) 18–22.

[24] N. Liang, J. Liu, S. Lin, Y. Wang, J.T. Wang, Y. Zhao, Y. Zhu, A multiscale architectured CuCrZr alloy with high strength, electrical conductivity and thermal stability, J. Alloy. Compd. 735 (2018) 1389–1394.

[25] A.H. Huang, Y.F. Wang, M.S. Wang, L.Y. Song, Y.S. Li, L. Gao, C.X. Huang, Y. T. Zhu, Optimizing the strength, ductility and electrical conductivity of a Cu-Cr-Zr alloy by rotary swaging and aging treatment, Mater. Sci. Eng. A 746 (2019) 211–216.

[26] I.S. Batra, G.K. Dey, U.D. Kulkarni, S. Banerjee, Precipitation in a Cu–Cr–Zr alloy, Mater. Sci. Eng. A 356 (2003) 32–36.

[27] U. Dahmen, Orientation relationships in precipitation systems, Acta Met. 30 (1982) 63–73.

[28] C.P. Luo, U. Dahmen, M.J. Witcomb, K.H. Westmacott, Precipitation in dilute Cu-Cr alloys: the effect of phosphorus impurities and aging procedure, Scr. Metal. Mater. 26 (1992) 649–654.